



# Silica nanowires encapsulated Ru nanoparticles as stable nanocatalysts for selective hydrogenation of CO<sub>2</sub> to CO

Jian Dou <sup>a</sup>, Yuan Sheng <sup>a</sup>, Catherine Choong <sup>b</sup>, Luwei Chen <sup>b</sup>, Hua Chun Zeng <sup>a,\*</sup>

<sup>a</sup> Department of Chemical and Biomolecular Engineering, Faculty of Engineering, National University of Singapore, 10 Kent Ridge Crescent, 119260, Singapore

<sup>b</sup> Institute of Chemical and Engineering Sciences, A\*STAR (Agency for Science, Technology and Research), 1 Pesek Road, Jurong Island, 627833, Singapore

## ARTICLE INFO

### Article history:

Received 16 March 2017

Received in revised form 29 June 2017

Accepted 27 July 2017

Available online 29 July 2017

### Keywords:

Mesoporous

Silica

Ru

Nanocatalyst

CO<sub>2</sub> hydrogenation

## ABSTRACT

Hydrogenation of carbon dioxide (CO<sub>2</sub>) to produce useful chemicals has been identified as a promising strategy for mitigation of greenhouse gas emission. Ruthenium (Ru) based catalysts have been reported to be the most active catalysts for the hydrogenation of CO<sub>2</sub> to methane (CH<sub>4</sub>) which unfortunately is also a greenhouse gas and is difficult to activate. Controlling the hydrogenation selectivity to produce carbon monoxide (CO), a direct precursor for enormous important chemicals, thus becomes desirable. However, achieving high CO selectivity with supported Ru catalysts has remained a challenging task. In this work, we report the synthesis of highly selective and stable Ru@mSiO<sub>2</sub> nanocatalysts via encapsulation of 1–3 nm Ru nanoparticles within mesoporous silica nanowires for hydrogenation of CO<sub>2</sub> to CO. Calcination of the catalyst in nitrogen prevented sintering of the encapsulated Ru nanoparticles, making high CO selectivity of up to 100% possible, while larger (5–20 nm) Ru particles resulting from calcination in air favored formation of CH<sub>4</sub>. DRIFTS study of 1–3 nm Ru@mSiO<sub>2</sub> and 5–20 nm Ru@mSiO<sub>2</sub> catalysts after adsorption of reaction mixture of H<sub>2</sub> and CO<sub>2</sub> reveals that different reaction intermediates form on catalyst surface: CO-Ru<sup>n+</sup> on 1–3 nm Ru@mSiO<sub>2</sub> and formate species on 5–20 nm Ru@mSiO<sub>2</sub>, which are responsible for the distinctively different selectivity observed on 1–3 nm Ru@mSiO<sub>2</sub> and 5–20 nm Ru@mSiO<sub>2</sub> catalysts. Plausible reaction pathways have been proposed for selective hydrogenation of CO<sub>2</sub> on the two types of catalysts, respectively. In addition, high CO selectivity of 1–3 nm Ru@mSiO<sub>2</sub> catalyst has been demonstrated to be stable.

© 2017 Elsevier B.V. All rights reserved.

## 1. Introduction

Carbon dioxide (CO<sub>2</sub>) is one of the major greenhouse gases, which poses impacts to the environment and sustainable growth of human society. [1–4] Mitigation of CO<sub>2</sub> emission amid climate change has therefore become a focus of research on sustainable development. In order to minimize carbon footprint, recycling of CO<sub>2</sub> has received enormous attention. Among other recognized technologies, utilization of captured CO<sub>2</sub> as feedstock for production of useful chemicals in a large scale is a feasible and economic strategy for reducing its emission. For instance, CO<sub>2</sub> has been used as additives (~5% in the feed stream) in industrial methanol synthesis processes. [5] For the large-scale utilization of CO<sub>2</sub>, it is desired to use pure CO<sub>2</sub> and hydrogen (H<sub>2</sub>) mixture for methanol synthesis, but design of efficient catalysts for hydrogenation of pure CO<sub>2</sub>

to methanol is particularly challenging. [1,6] Alternatively, CO<sub>2</sub> can be firstly hydrogenated to carbon monoxide (CO) through reverse water gas shift reaction (RWGS, CO<sub>2</sub> + H<sub>2</sub> ↔ CO + H<sub>2</sub>O). The resulting CO<sub>2</sub>/CO/H<sub>2</sub> mixture can be used as the feed for methanol synthesis. [7] In fact, selective hydrogenation of CO<sub>2</sub> to CO has been identified as one of the most promising process for CO<sub>2</sub> utilization, as the CO product is the feedstock for C1 chemistry. [1,4]

There have been many catalysts such as supported copper, nickel, platinum, palladium, rhodium and ruthenium developed for CO<sub>2</sub> hydrogenation at atmospheric pressure. [8–32] Copper based catalysts have been extensively studied for hydrogenation of CO<sub>2</sub> due to their excellent activity and selectivity. For example, Cu/SiO<sub>2</sub> catalyst with Cu nanoparticles of 2.4 nm has been prepared by atomic layer epitaxy technique, which shows comparable activity as Pt/SiO<sub>2</sub> catalyst for CO<sub>2</sub> hydrogenation. [10] Recently, Cu/β-Mo<sub>2</sub>C catalyst prepared by temperature-programmed carburation method significantly improves the dispersion of Cu and exhibits superior activity comparing to Pt based catalysts. [24] Noble metal based catalysts have also been widely studied for

\* Corresponding author.

E-mail address: [chezhc@nus.edu.sg](mailto:chezhc@nus.edu.sg) (H.C. Zeng).

hydrogenation of  $\text{CO}_2$ , due to excellent activity and stability. For instance, Ru-based catalysts deposited on various catalyst supports (e.g.,  $\text{TiO}_2$ ,  $\text{CeO}_2$  and  $\text{Co}_3\text{O}_4$ ) have also been investigated for hydrogenation of  $\text{CO}_2$  to  $\text{CH}_4$ . [20–23] Particularly, 0.8%Ru/ $\text{TiO}_2$  with Ru particle size of 2.5 nm prepared via sputter coating was reported to be extremely active for  $\text{CH}_4$  production from  $\text{CO}_2$  even at 200 °C. [23] Since  $\text{CH}_4$  itself is also a greenhouse gas, selective hydrogenation of  $\text{CO}_2$  to CO (instead of  $\text{CH}_4$ ) becomes a challenging research in this field. For instance, homogeneous Ru catalysts such as mononuclear Ru halogen carbonyl complexes, triruthenium dodecacarbonyl bis(triphenylphosphine)iminium chloride ( $\text{Ru}_3(\text{CO})_{12}\text{-[PPN]Cl}$ ) and potassium ruthenium ethylenediaminetetraacetic acid chloride ( $\text{K}[\text{Ru-(H-EDTA)Cl}]$ ) have been employed for reduction of  $\text{CO}_2$  to CO at very high pressure (30–80 bar). [33–35] On the other hand, Ru-based heterogeneous catalysts such as 2%Ru/ $\text{SiO}_2$  have been investigated for hydrogenation of  $\text{CO}_2$ , with CO selectivity of less than 50% at  $\text{CO}_2$  conversion of 20%. [36] High initial CO selectivity has been achieved with 0.1%Ru/ $\text{Al}_2\text{O}_3$  catalyst, but it dropped to less than 50% after 4 h of reaction. [37] Thus it remains difficult to prepare highly selective Ru nanocatalysts for RWGS reaction. In addition, the catalyst stability has to be further enhanced for production of CO from  $\text{CO}_2$ .

Mesoporous silica has been widely used as catalyst support for noble metal catalysts owing to uniform pore structure and high surface area. [38–40] In this work, we utilized silica nanowires with bimodal pore structure for synthesizing Ru@ $\text{mSiO}_2$  nanocatalysts for RWGS reaction and investigated the influence of size of the Ru nanoparticles on the reaction yield and product selectivity. Briefly, two types of Ru-based nanocatalysts have been prepared by encapsulation of pre-synthesized Ru nanoparticles with mesoporous silica nanowires (Fig. 1). The prepared Ru@ $\text{mSiO}_2$  nanowires were further thermally treated in nitrogen to generate stable 1–3 nm Ru@ $\text{mSiO}_2$  nanocatalysts. When heated in air, the as-synthesized Ru@ $\text{mSiO}_2$  was transformed into Ru $\text{O}_2$ @ $\text{mSiO}_2$ , and then reduced by  $\text{H}_2/\text{CO}_2$  mixture to form 5–20 nm Ru@ $\text{mSiO}_2$  nanocatalysts. These two groups of nanocatalysts (i.e., 1–3 nm Ru@ $\text{mSiO}_2$  and 5–20 nm Ru@ $\text{mSiO}_2$ ) were investigated as hydrogenation catalysts for selective reduction of  $\text{CO}_2$  to CO or  $\text{CH}_4$  respectively.

## 2. Experimental section

### 2.1 Preparation of ruthenium nanoparticles

Ru nanoparticles were prepared by a polyol-assisted method following literature procedures with some modifications. [40,41] In a typical synthesis, for example, 0.10 g of Ruthenium (III) chloride hydrate ( $\text{RuCl}_3\text{-xH}_2\text{O}$ , 99.98%, Sigma-Aldrich) and 0.20 g of sodium hydroxide ( $\text{NaOH}$ , 99 +%, Merck) were dissolved in 50 mL of ethylene glycol (EG,  $\text{C}_2\text{H}_6\text{O}_2$ , 99.5 +%, Merck) by heating at 80 °C for 30 min. The resulting light brown solution was further heated at 160 °C under reflux for 3 h. After the reaction, the mixture was cooled to room temperature and stored for further use.

### 2.2 Preparation of Ru@ $\text{mSiO}_2$ nanowires

Basic steps of preparing Ru@ $\text{mSiO}_2$  nanowires could be considered similar to a literature method for pure mesoporous silica ( $\text{mSiO}_2$ ) nanowires. [42] However, a major modification was made to incorporate Ru nanoparticles. Briefly, 13 mL of deionized water was mixed with 1 mL of ethanol, followed by addition of 2 mL of hexadecyltrimethylammonium chloride solution (CTACl, 25 wt.% in  $\text{H}_2\text{O}$ , Sigma-Aldrich), 0.5 mL of triethanolamine (TEA,  $\text{C}_6\text{H}_{15}\text{NO}_3$ , 99 +%, Acros Organics), and 1–5 mL of Ru colloidal suspension (prepared by the above procedure). The resulting mixture was stirred at room temperature for 30 min. After that, 0.5 mL of tetraethyl orthosilicate (TEOS,  $\text{Si}(\text{OC}_2\text{H}_5)_4$ , 99.0 +%, Sigma-Aldrich) was added dropwise to the above mixture. The mixture was further stirred for 5 min, followed by heating at 60 °C in an electric oven for 2 h.

The final product was collected by centrifuging and washed with ethanol. The as-synthesized catalysts are denoted as Ru@ $\text{mSiO}_2\text{-X}$ , where X = 1, 3, and 5; the number corresponds to the amount (volume in mL) of Ru colloid solution used for synthesis.

### 2.3 Preparation of 1–3 nm Ru@ $\text{mSiO}_2$ and 5–20 nm Ru@ $\text{mSiO}_2$ catalysts

The aforementioned Ru@ $\text{mSiO}_2$  nanowires were calcined at 400 °C for 6 h (heating rate 1 °C/min) in 30 mL/min of  $\text{N}_2$  flow to generate 1–3 nm Ru@ $\text{mSiO}_2$  catalysts (samples are named 0.4, 1.6 or 2.7% Ru@ $\text{mSiO}_2\text{-N}$  according to measured Ru loading, where "N" stands for nitrogen). To prepare 5–20 nm Ru@ $\text{mSiO}_2$  nanocatalysts, the as-synthesized Ru@ $\text{mSiO}_2$  nanowires were calcined at 400 °C for 6 h in static laboratory air, followed by reduction at 400 °C for 2 h with 25 mL/min of  $\text{H}_2/\text{CO}_2$  flow ( $\text{H}_2:\text{CO}_2$  = 4:1 mol/mol), and the products are denoted by 0.4, 1.7 or 3.0%Ru@ $\text{mSiO}_2\text{-A}$  according to Ru loading, where "A" stands for air. The reduced 1.6%Ru@ $\text{mSiO}_2\text{-N-H}$  catalyst was prepared by heating 1.6%Ru@ $\text{mSiO}_2\text{-N}$  sample at 600 °C in 10% $\text{H}_2/\text{N}_2$  to remove surface carbon species.

### 2.4 Hydrogenation of $\text{CO}_2$

Hydrogenation of  $\text{CO}_2$  was carried out in a fixed bed stainless steel reactor (inner diameter = 7 mm, length = 50 cm). Catalyst bed at the center of the reactor was supported by glass wool at both ends, while the remaining space was filled with 2 mm glass beads. Temperature was measured by a type K thermocouple inserted into the reactor and near the catalyst bed. Gas mixture of  $\text{H}_2$  and  $\text{CO}_2$  ( $\text{H}_2:\text{CO}_2$  = 4:1) at a total flow rate of 25 mL/min was fed into the reactor. The reaction temperature was increased from 100 to 400 °C with 50 or 25 °C intervals. Reactants and products were monitored by gas chromatography (GC, Agilent-7890A) coupled with flame ionization detector (FID) and thermal conductivity detector (TCD).

### 2.5 Materials characterization

Crystallographic structures of Ru@ $\text{mSiO}_2$  catalysts were characterized by powder X-ray diffraction (XRD, Bruker D8 Advance,  $\text{Cu K}_\alpha$  radiation,  $\lambda = 1.5406 \text{ \AA}$ ) at a scanning rate of 1 °/min. Morphology and dimension of the catalyst samples were examined by transmission electron microscopy (TEM, JEM2010, 200 kV), and high resolution transmission electron microscopy (HRTEM, JEM2100F, 200 kV). Ru loading was determined by atomic emission spectroscopy with inductively coupled plasma as excitation source (ICP-AES, PerkinElmer Optima 5300DV), and carbon content by CHNS analysis (Elementar Vario MICRO cube). Textural properties (e.g., specific surface area, pore size, and pore volume, etc.) were studied by nitrogen adsorption-desorption analysis (Quantachrome NOVA-3000) at 77 K. Prior to  $\text{N}_2$  adsorption analysis, the samples were degassed at 200 °C overnight with He flow. X-ray photoelectron spectroscopy (XPS, AXIS Ultra DLD, Kratos Analytical) with  $\text{Al K}_\alpha$  exciting radiation ( $h\nu = 1486.71 \text{ eV}$ ) was also used to probe surface compositions and chemical states of Ru@ $\text{mSiO}_2$  nanocatalysts. All binding energies (BEs) were referenced to the Si 2p peak (BE = 103.3 eV) from the mesoporous silica nanowire support. Temperature-programmed reduction (TPR) and temperature-programmed desorption (TPD) were performed using a TPDRO 1100 Series (Thermo Electron). For TPR analysis, 35–70 mg of sample was heated from 22 to 600 °C (heating rate 10 °C/min) in 50 mL/min of a 5%  $\text{H}_2/\text{Ar}$  flow. TPD measurement was carried out after TPR analysis. 50 mL/min of 5%  $\text{H}_2/\text{Ar}$  was passed through the reduced sample at 30 °C for 30 min, followed by flushing with Ar for 30 min. After that, the sample was ramped from 30 to 600 °C at a heating rate of 10 °C/min under Ar (50 mL/min). *In-situ* diffuse reflectance infrared Fourier transform spectroscopy (DRIFTS) experiments were performed in a Perkin Elmer Frontier FTIR spectrometer equipped with a high temperature cell fitted with ZnSe windows and with a mercury-cadmium-telluride (MCT-A) detector which was cooled with liquid nitrogen. Spectra were acquired at a resolution of  $4 \text{ cm}^{-1}$  and typically over 256 scans. The catalyst was first reduced in a  $\text{H}_2$  flow (50 mL/min) at 400 °C for 2 h and cooled

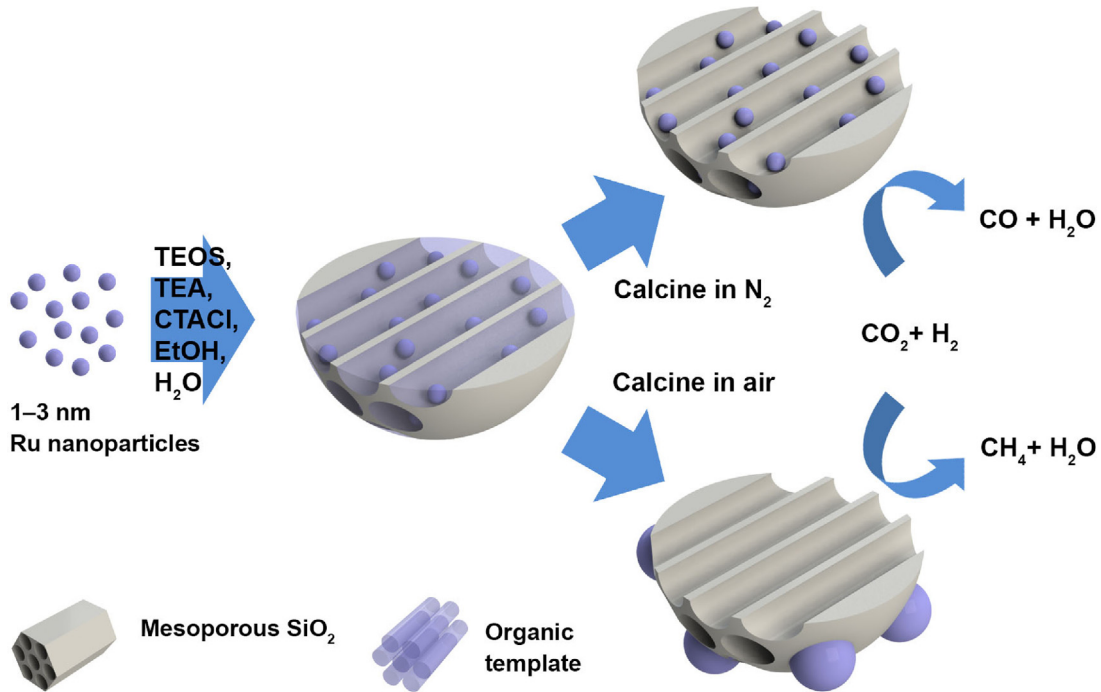


Fig. 1. Schematic representation of the synthesis of Ru@mSiO<sub>2</sub> nanocatalysts for selective reduction of CO<sub>2</sub> to either CO or CH<sub>4</sub>.

under a He flow (50 mL/min) to 30 °C. Subsequently, reactant gas mixture of H<sub>2</sub> and CO<sub>2</sub> (H<sub>2</sub>:CO<sub>2</sub> = 4:1) was introduced into the reaction cell which was heated up from 30 to 400 °C. The spectra were taken at 50 °C intervals after 10 min of stabilization. A spectrum of the sample recorded just after reduction was used as a reference.

### 3. Results and discussion

**3.1 Controlling metal content and particle size for Ru@mSiO<sub>2</sub> nanowires.** The integrated mesoporous silica nanowires-encapsulated ruthenium nanocatalysts had tunable sizes depending on synthesis conditions. Figs. S1–S3 show that the diameter of silica nanowires increased from ~20 to ~40 nm as the amount of Ru colloidal suspension added during synthesis increased from 1 to 5 mL. The observation is consistent with our previous report that diameter of silica nanowires becomes larger with increasing amount of ethanol used for synthesis. [42] It should be mentioned that the colloidal suspension of Ru nanoparticles (used as a ruthenium metal source) consisted predominantly of ethylene glycol. In this work, ethylene glycol had similar function as ethanol and affected the morphology of emulsion template in the synthesis solution. As a result, Ru nanoparticles with the size of around 1–3 nm were uniformly integrated into silica nanowires. The metal content in the catalysts could be easily controlled; an increased volume of the Ru colloid during synthesis led to a higher population of Ru nanoparticles in the Ru@mSiO<sub>2</sub> nanowire products.

The as-prepared Ru@mSiO<sub>2</sub> nanowires were calcined either in static air or under a flow of nitrogen to remove the organic template (CTACl). After calcination in N<sub>2</sub> at 400 °C, the size of encapsulated Ru nanoparticles remained almost unchanged as 1–3 nm (Fig. 2a,b, Fig. 3a,c, and Figs. S4–S6). Shown in Fig. 2b, the lattice fringes with interspaces of 0.21 and 0.23 nm can be assigned to (101) and (100) planes of hexagonal Ru (JCPDS 89–4903). In contrast, larger nanocrystals with sizes of 5–30 nm formed if the Ru@mSiO<sub>2</sub> nanowires were calcined in air (Fig. 2c,d, Fig. 3b,d, and Figs. S7–S9). A nanocrystal of this type is displayed in Fig. 2d (with a size of 25 nm). The observed lattice fringes with interspaces of 0.32 and

0.25 nm are attributed to the (110) and (101) planes of tetragonal RuO<sub>2</sub> phase (JCPDS 43–1027). More such RuO<sub>2</sub> nanocrystals were observed as Ru content increased from 0.4% to 3.0% (Figs. S7–S9). The formation of RuO<sub>2</sub> nanocrystals is due to oxidative sintering of pristine Ru nanoparticles in air. There are basically two mechanisms (i.e., particulate coalescence and Ostwald ripening) accounting for sintering of nanocatalysts. [43,44] The particulate coalescence refers to sintering *via* migration of nanoparticles followed by coalescence of neighboring nanoparticles, and the Ostwald ripening to sintering *via* diffusive deposition of atomic species from small nanoparticles to bigger ones. Both mechanisms are plausible for forming larger RuO<sub>2</sub> nanocrystals when the metallic Ru nanoparticles are heated and oxidized in air. On the other hand, the organic template (CTACl) may decompose to form carbon species in the N<sub>2</sub> atmosphere and remain on the surface of Ru nanoparticles to hinder their migration and thus coalescence. After *in-situ* reduction at 400 °C for 2 h in H<sub>2</sub>/CO<sub>2</sub> mixture, the Ru particle size of N<sub>2</sub>-treated sample remained small at 1–3 nm (Fig. 4a,b). The lattice spacing of 0.21 nm can be assigned to the (101) planes of metallic Ru. Shown in Fig. 4c,d, the size of RuO<sub>2</sub> nanocrystals shrank to 5–20 nm after reduction with the same H<sub>2</sub>/CO<sub>2</sub>. The lattice spacing of 0.21 nm belongs to the (101) planes of metallic Ru, indicating reductive conversion of RuO<sub>2</sub> to the metal.

The textural properties of Ru@mSiO<sub>2</sub> nanowires were investigated by N<sub>2</sub> adsorption and desorption analysis (Fig. 5). Type IV isotherms associated with type H1 hysteresis loops were observed for all the Ru@mSiO<sub>2</sub> samples calcined either in air or in N<sub>2</sub>. The initial uptake of N<sub>2</sub> at below relative pressure of 0.1 is ascribed to monolayer adsorption of N<sub>2</sub>. The adsorption step at 0.2–0.4 is typically associated with mesoporous materials due to capillary condensation. The hysteresis loop at 0.8–1.0 is assigned to condensation in void space between the silica nanowires. For Ru@mSiO<sub>2</sub>-N samples, the BET surface areas decrease from 968 to 912 m<sup>2</sup>/g as the amount of Ru colloidal suspension used increases from 1 to 3 mL. Further increase in Ru content has negligible effect on surface area (Table 1). The BET surface areas of Ru@mSiO<sub>2</sub>-A samples are similar to those of Ru@mSiO<sub>2</sub>-N samples, indicating both methods of calcination are effective in removing the organic template.

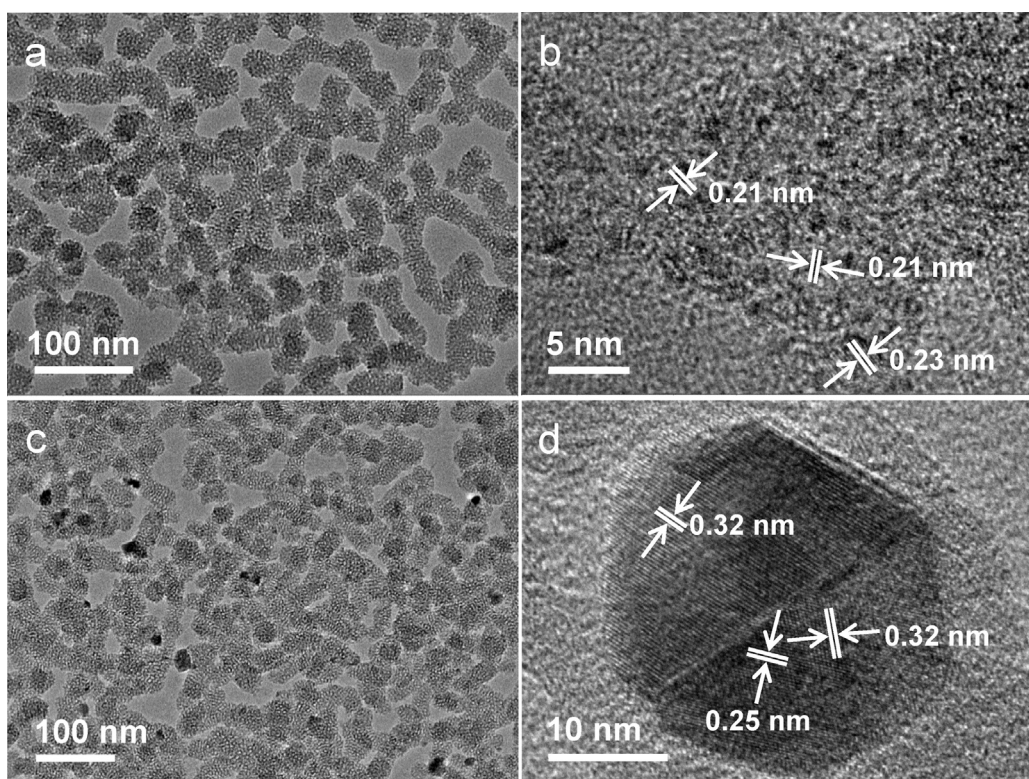


**Fig. 2.** TEM/HRTEM images of (a,b) 1.6%Ru@mSiO<sub>2</sub>-N nanowires calcined in nitrogen and (c,d) 1.7%Ru@mSiO<sub>2</sub>-A nanowires calcined in air before reduction.

**Table 1**  
Hydrogenation of CO<sub>2</sub> with Ru@mSiO<sub>2</sub> catalysts.<sup>a</sup>

Entry	Catalyst	Ru loading <sup>b</sup> (%)	S <sub>BET</sub> (m <sup>2</sup> /g)	Temp. (°C)	CO <sub>2</sub> conv. (%)	CO sel. (%)	TOF <sup>c</sup> (s <sup>-1</sup> )	Apparent activation energy <sup>d</sup> (kJ/mol)
1	0.4%Ru@mSiO <sub>2</sub> -N	0.4	968	400	13.7	93.4	0.127	81 ± 3
				350	4.4	100	0.04	
2	1.6%Ru@mSiO <sub>2</sub> -N	1.6	912	400	23.0	83.5	0.053	80 ± 3
				350	9.4	88.1	0.02	
3	1.6%Ru@mSiO <sub>2</sub> -N-H <sup>e</sup>	1.6	912	400	20.6	93.6	0.047	–
4	2.7%Ru@mSiO <sub>2</sub> -N	2.7	915	400	25.9	72.4	0.035	89 ± 5
5	0.4%Ru@mSiO <sub>2</sub> -A	0.4	984	400	13.7	70.4	0.127	78 ± 3
6	1.7%Ru@mSiO <sub>2</sub> -A	1.7	898	400	19.9	4.8	0.043	75 ± 5
7	3.0%Ru@mSiO <sub>2</sub> -A	3.0	895	400	21.0	4.6	0.026	78 ± 3
8	1.4%Ru/TiO <sub>2</sub> <sup>f</sup>	1.4	52	200	80	0	0.025	–
9	(Co <sub>0.95</sub> Ru <sub>0.05</sub> ) <sub>3</sub> O <sub>4</sub> <sup>g</sup>	5.0	–	300	25	1.0	–	–
10	Ce <sub>0.99</sub> Ru <sub>0.01</sub> O <sub>2</sub> <sup>h</sup>	1.0	–	500	16	10.0	0.12	–
11	2.0%Ru/SiO <sub>2</sub> <sup>i</sup>	2.0	490	350	15	47.0	0.054	–
12	0.1%Ru/Al <sub>2</sub> O <sub>3</sub> <sup>j</sup>	0.1	200	350	2.5	34.8	0.112	82 (CO), 62 (CH <sub>4</sub> )
13	9%Cu/1.9%K/SiO <sub>2</sub> <sup>k</sup>	9 <sup>l</sup>	–	500	3.4	–	0.045	–
14	1%Pt/Al <sub>2</sub> O <sub>3</sub> <sup>m</sup>	0.97 <sup>n</sup>	146	400	20	–	0.125	–
15	2%Pt/TiO <sub>2</sub> <sup>o</sup>	2.0 <sup>o</sup>	21	400	21	88	0.137	–
16	2.4%Au/UiO-67 <sup>p</sup>	2.4 <sup>q</sup>	725	408	2	–	0.006	–

<sup>a</sup> Reaction conditions: 100 mg of catalyst, 25 mL/min of H<sub>2</sub>/CO<sub>2</sub> (4:1) gas mixture, weight hours space velocity (WHSV) = 15,000 mL h<sup>-1</sup> g<sup>-1</sup>, temperature (T) = 200–400 °C.

<sup>b</sup> Ru loading was measured by ICP-AES.

<sup>c</sup> TOF was calculated as mole of CO<sub>2</sub> converted per mole of total metal per second.

<sup>d</sup> Apparent activation energy for CO<sub>2</sub> conversion was calculated using Arrhenius equation based on results from Fig. 8.

<sup>e</sup> 1.6%Ru@mSiO<sub>2</sub>-N-H catalyst was prepared by reducing 1.6%Ru@mSiO<sub>2</sub>-N sample at 600 °C for 2 h in 50 mL/min of 10%H<sub>2</sub>/N<sub>2</sub> flow.

<sup>f</sup> from ref 20.

<sup>g</sup> from ref 21.

<sup>h</sup> from ref 22.

<sup>i</sup> from ref 36.

<sup>j</sup> from ref 37, with selectivity calculated from Fig. 2a in ref 37.

<sup>k</sup> from ref 47.

<sup>l</sup> Cu loading (%).

<sup>m</sup> from ref 48.

<sup>n</sup> Pt loading (%).

<sup>o</sup> from ref 49.

<sup>p</sup> from ref 50.

<sup>q</sup> Au loading.

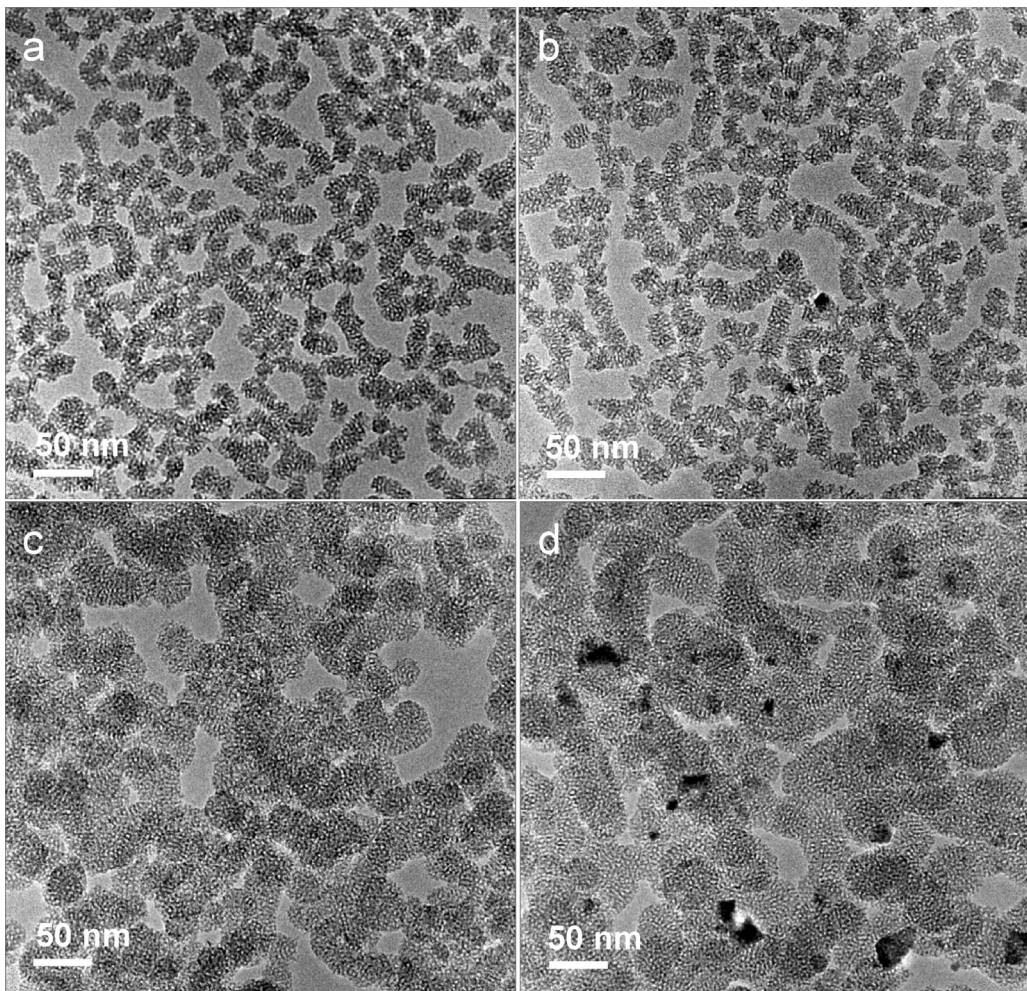


**Fig. 3.** TEM images of freshly calcined catalysts: (a) 0.4%Ru@mSiO<sub>2</sub>-N, (b) 0.4%Ru@mSiO<sub>2</sub>-A, (c) 2.7%Ru@mSiO<sub>2</sub>-N, and (d) 3.0%Ru@mSiO<sub>2</sub>-A. The Ru@mSiO<sub>2</sub>-A samples were examined before reduction.

Mesopore size was determined to be 4.1 nm for the six samples by nonlocal density function theory (NLDFT) method, which is large enough for accommodation of the small Ru nanoparticles within the mesopores. [45]

As-prepared and calcined Ru@mSiO<sub>2</sub> nanowires were characterized by powder XRD technique to determine the crystallinity of encapsulated nanoparticles (Fig. 6a and Fig. S10). No diffraction peak corresponding to the loaded Ru was observed for the as-prepared Ru@mSiO<sub>2</sub> samples because the Ru nanoparticles were too small to be detected by XRD, which is consistent with TEM observation. After calcination in N<sub>2</sub>, all the three samples exhibited similar XRD patterns as those of the as-prepared samples (Fig. 6a). It further confirms the effectiveness of N<sub>2</sub> atmosphere in preserving the small particle size of Ru upon heating. In comparison, calcination in static air led to formation of RuO<sub>2</sub>: peaks at  $2\theta = 28.2^\circ$ ,  $35.3^\circ$  and  $54.5^\circ$  were observed for the three Ru@mSiO<sub>2</sub>-A samples (Fig. 6a), which can be assigned to the (110), (101), and (211) reflections of RuO<sub>2</sub> with a rutile structure (tetragonal; JCPDS card 43–1027, space group:  $P4_2/mnm$ ,  $a_0 = b_0 = 4.499$  Å, and  $c_0 = 3.107$  Å).

XPS analysis was carried out to study the oxidation states of Ru in the as-synthesized and calcined samples, as displayed in Figs. S11–S13. All the binding energies were referenced to Si 2p (103.3 eV). Ru 3p peaks were used for analysis, since Ru 3d peaks were very close to C 1s peaks. Taking the as-prepared Ru@mSiO<sub>2</sub>-3 as an example (Fig. S11), the Ru 3p<sub>3/2</sub> peak at 462.5 eV is attributed to Ru<sup>4+</sup> of RuO<sub>2</sub>. [22] It reveals that the surface of Ru nanopar-

ticles was oxidized in our synthesis. In the O 1s spectrum, the first peak at 530.7 eV is attributed to lattice oxygen of the surface RuO<sub>2</sub> and silica, the second peak at 532.6 eV is assigned to the oxygen of surface hydroxyl groups, and the last peak at 533.9 eV to chemisorbed oxygen molecules and/or oxygen of adsorbed water molecules. After calcination of the as-synthesized Ru@mSiO<sub>2</sub>-3 in N<sub>2</sub>, the Ru 3p<sub>3/2</sub> peak shifted downward to 461.8 eV (Fig. S12b), which can be assigned to metallic Ru. [46] It indicates that the surface oxide of encapsulated Ru nanoparticles was reduced by the organic template. When the as-synthesized Ru@mSiO<sub>2</sub>-3 sample was calcined in air, on the other hand, the embedded Ru nanoparticles were oxidized to RuO<sub>2</sub>, as the Ru 3p<sub>3/2</sub> peak shifted upward to 462.7 eV (Fig. S13b). [22] These XPS results are highly consistent with our TEM and XRD findings in Figs. 2 and 4 and Fig. 6.

**3.2 Hydrogenation of CO<sub>2</sub>.** The above calcined samples have been investigated as catalysts for CO<sub>2</sub> hydrogenation. As shown in Fig. 7a, there was no reaction for all the six catalysts in the temperature range of 100–225 °C. CO<sub>2</sub> conversion increased with temperature from 250 to 400 °C. For the Ru@mSiO<sub>2</sub>-N samples, the conversion of CO<sub>2</sub> at 400 °C increased from 13.7% to 25.9% with increase in Ru content from 0.4% to 2.7% (Fig. 7a and Table 1). Similar trends were also observed for the Ru@mSiO<sub>2</sub>-A samples, since more active sites were available for the reaction with higher Ru loadings. However, turnover frequencies (TOF; defined as moles of CO<sub>2</sub> converted per mole of the loaded Ru per second) of catalysts decreased with Ru loading. This is due to lower percentage of exposed Ru sur-

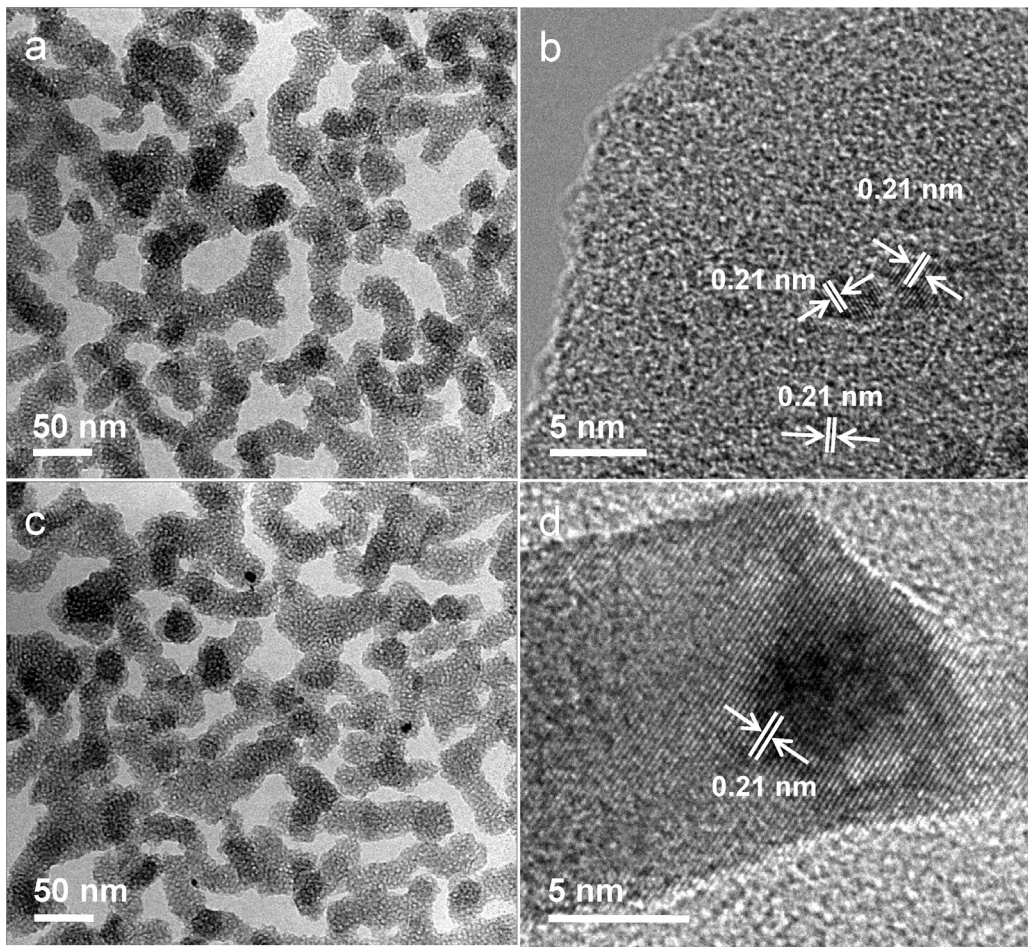


**Fig. 4.** TEM/HRTEM images of (a,b) 1.6%Ru@mSiO<sub>2</sub>-N nanowires and (c,d) 1.7%Ru@mSiO<sub>2</sub>-A nanowires after reduction with H<sub>2</sub>/CO<sub>2</sub> mixture at 400 °C for 2 h.

face in samples with higher Ru loading. For Ru@mSiO<sub>2</sub>-1 samples, calcination in air or N<sub>2</sub> has little effect on the activity of catalysts. However, for samples with higher Ru loading, calcination in N<sub>2</sub> is beneficial to hydrogenation activity, particularly at high reaction temperatures. For example, the conversion of CO<sub>2</sub> at 400 °C was 23.0% and 19.9% for 1.6%Ru@mSiO<sub>2</sub>-N and 1.7%Ru@mSiO<sub>2</sub>-A catalysts, respectively. As explained earlier, the particle size of Ru nanocrystals in reduced Ru@mSiO<sub>2</sub>-A is larger compared to that in Ru@mSiO<sub>2</sub>-N samples, leading to fewer active sites. It is noted that the activity of 0.4%Ru@mSiO<sub>2</sub>-N catalyst is 0.127 s<sup>-1</sup> at 400 °C, which is comparable to or higher than that of 9%Cu/1.9%K/SiO<sub>2</sub> (0.045 s<sup>-1</sup> at 500 °C), 1%Pt/Al<sub>2</sub>O<sub>3</sub> (0.125 s<sup>-1</sup> at 400 °C), 2%Pt/TiO<sub>2</sub> (0.137 s<sup>-1</sup> at 400 °C), and 2.4%Au/UIO-67 (0.006 s<sup>-1</sup> at 408 °C) catalysts (Table 1, entry 1 vs. entries 13–16).<sup>[47–50]</sup>

It was observed that the selectivity of CO over CH<sub>4</sub> varied with the Ru content in these catalysts (Fig. 7b and Table 1). For Ru@mSiO<sub>2</sub>-N, the CO selectivity at 400 °C decreased from 93.4% to 72.4% with increasing Ru loading from 0.4% to 2.7%. Similarly, the CO selectivity for Ru@mSiO<sub>2</sub>-A decreased from 70.4% to 4.6% at 400 °C with increasing Ru from 0.4% to 3.0%. It seems that lower Ru contents favor the production of CO instead of CH<sub>4</sub>. However, the CO selectivity of Ru@mSiO<sub>2</sub>-N and Ru@mSiO<sub>2</sub>-A catalysts differs dramatically even with similar Ru loading. For instance, the selectivity of CO for 1.6%Ru@mSiO<sub>2</sub>-N and 1.7%Ru@mSiO<sub>2</sub>-A catalysts was 83.5% and 4.8% respectively at 400 °C, while the Ru loadings in these two samples were very similar (1.6–1.7% according to ICP analysis). To compare the selectivity at similar conversion of CO<sub>2</sub> (e.g., 10 ± 2%), the CO selectivity for 0.4, 1.6, and 2.7%Ru@mSiO<sub>2</sub>-N catalysts was 100, 88.1 and 82.6%, while the

selectivity of CO for 0.4, 1.7, and 3.0%Ru@mSiO<sub>2</sub>-A catalysts was 66.7, 14.2, and 9.7% respectively at 350 °C. It is noticed that most of the Ru catalysts reported in the literature catalyze hydrogenation of CO<sub>2</sub> mainly to form CH<sub>4</sub>, with selectivity of CO lower than 50% (Entries 8–12, Table 1).<sup>[20–22,36,37]</sup> This clearly demonstrates the unique advantage of Ru@mSiO<sub>2</sub>-N catalysts in selective production of CO from CO<sub>2</sub>. In particular, 0.4%Ru@mSiO<sub>2</sub>-N exhibited 100% selectivity toward CO at 350 °C. From previous TEM and HRTEM observations, it is known that the encapsulated Ru nanoparticles remained small with sizes of 1–3 nm after calcination in N<sub>2</sub>. Larger Ru nanocrystals (5–20 nm) were associated with reduced Ru@mSiO<sub>2</sub>-A samples. We can conclude that 1–3 nm Ru nanoparticles favor the formation of CO, while 5–20 nm Ru nanocrystals are selective toward CH<sub>4</sub>. To confirm this conclusion, the nitrogen treated catalyst (i.e., 1.6%Ru@mSiO<sub>2</sub>-N) was further reduced at 600 °C in 10%H<sub>2</sub>/N<sub>2</sub> to remove any surface carbon species. The resulting 1.6%Ru@mSiO<sub>2</sub>-N-H catalyst was investigated for CO<sub>2</sub> hydrogenation activity. As shown in entry 3 of Table 1 and Fig. S14, the conversion of CO<sub>2</sub> at 400 °C was 20.6%, which is comparable with untreated 1.6%Ru@mSiO<sub>2</sub>-N catalyst. The selectivity of CO reached 93.6%, which is higher than that of 1.6%Ru@mSiO<sub>2</sub>-N catalyst. It suggests that surface carbon species have no promotion effect on the selectivity of CO formation, and small Ru nanoparticles are critical for selective hydrogenation of CO<sub>2</sub> to CO. Our current observation is also consistent with a recent investigation on Ru/Al<sub>2</sub>O<sub>3</sub> catalysts which proposed that active sites for CO formation are highly dispersed single ruthenium atoms (these form CO with high selectivity) and possibly related small metal aggregates as well.<sup>[37]</sup>

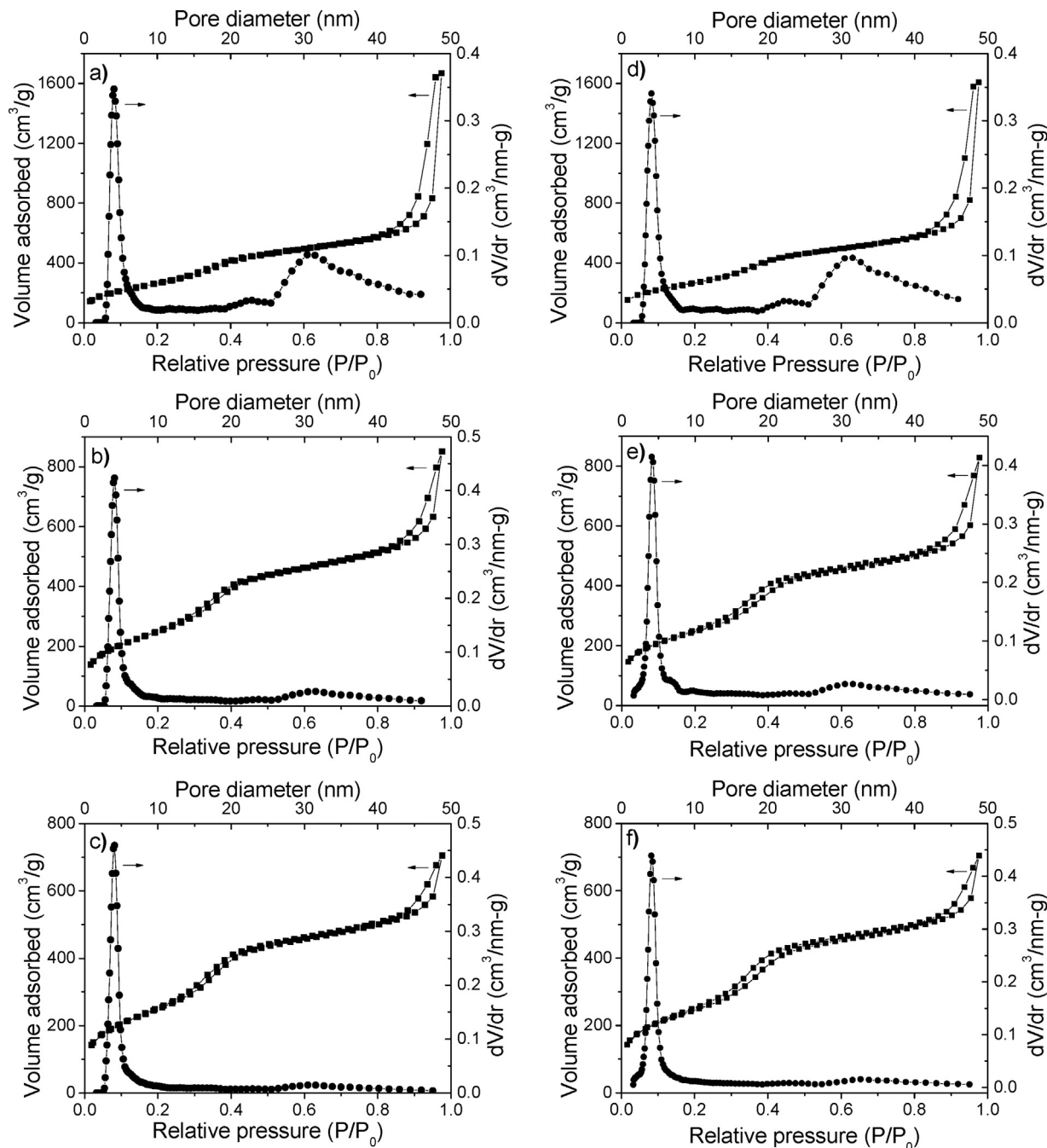


**Fig. 5.**  $\text{N}_2$  adsorption-desorption isotherms and pore size distributions of freshly calcined catalysts: (a) 0.4%Ru@mSiO<sub>2</sub>-N, (b) 1.6%Ru@mSiO<sub>2</sub>-N, (c) 2.7%Ru@mSiO<sub>2</sub>-N, (d) 0.4%Ru@mSiO<sub>2</sub>-A, (e) 1.7%Ru@mSiO<sub>2</sub>-A, and (f) 3.0%Ru@mSiO<sub>2</sub>-A.

**Fig. 8** presents the Arrhenius-type plot for Ru@mSiO<sub>2</sub>-N and Ru@mSiO<sub>2</sub>-A catalysts. The apparent activation energies for  $\text{CO}_2$  conversion were found to be 80–89 kJ/mol for Ru@mSiO<sub>2</sub>-N, which are generally higher than those for Ru@mSiO<sub>2</sub>-A catalysts (75–78 kJ/mol). As major products from Ru@mSiO<sub>2</sub>-N and Ru@mSiO<sub>2</sub>-A catalysts are CO and  $\text{CH}_4$  respectively, it suggests that the apparent activation energy of CO formation is higher than that of  $\text{CH}_4$  generation. The apparent activation energies for formations of CO and  $\text{CH}_4$  were further measured for our 0.4%Ru@mSiO<sub>2</sub>-A to be  $79 \pm 2$  and  $69 \pm 4$  kJ/mol respectively. The measured apparent activation energies are comparable with literature results for 0.5–5%Ru/Al<sub>2</sub>O<sub>3</sub> (82 kJ/mol for CO formation and 62 kJ/mol for  $\text{CH}_4$  formation), and 0.5%Ru/SiO<sub>2</sub> (72 kJ/mol for  $\text{CO}_2$  conversion and  $\text{CH}_4$  formation).<sup>[37,51]</sup>

The reducibility of 1.6%Ru@mSiO<sub>2</sub>-N and 1.7%Ru@mSiO<sub>2</sub>-A was investigated by temperature-programmed reduction (Fig. 6c). The first reduction peaks appeared at 85 and 151 °C for 1.6%Ru@mSiO<sub>2</sub>-N and 1.7%Ru@mSiO<sub>2</sub>-A, respectively, further confirming that the encapsulated Ru nanoparticles were fully reduced to metallic state during the hydrogenation reaction at 250–400 °C. It is known that silica supported ruthenium catalysts can generally be reduced at below 300 °C.<sup>[52,53]</sup> The broad reduction peak centered at 515 °C which only occurred for the nitrogen-treated catalyst could be due to hydrogenation of deposited carbon species, as suggested by results of elemental analysis for 1.6%Ru@mSiO<sub>2</sub>-N (0.92 wt% carbon) and 1.7%Ru@mSiO<sub>2</sub>-A (<0.5% carbon). It has been reported that surface carbon fibers and whiskers could be removed by hydrogenation at 400–600 °C, and surface graphitic carbon at 550–850 °C.

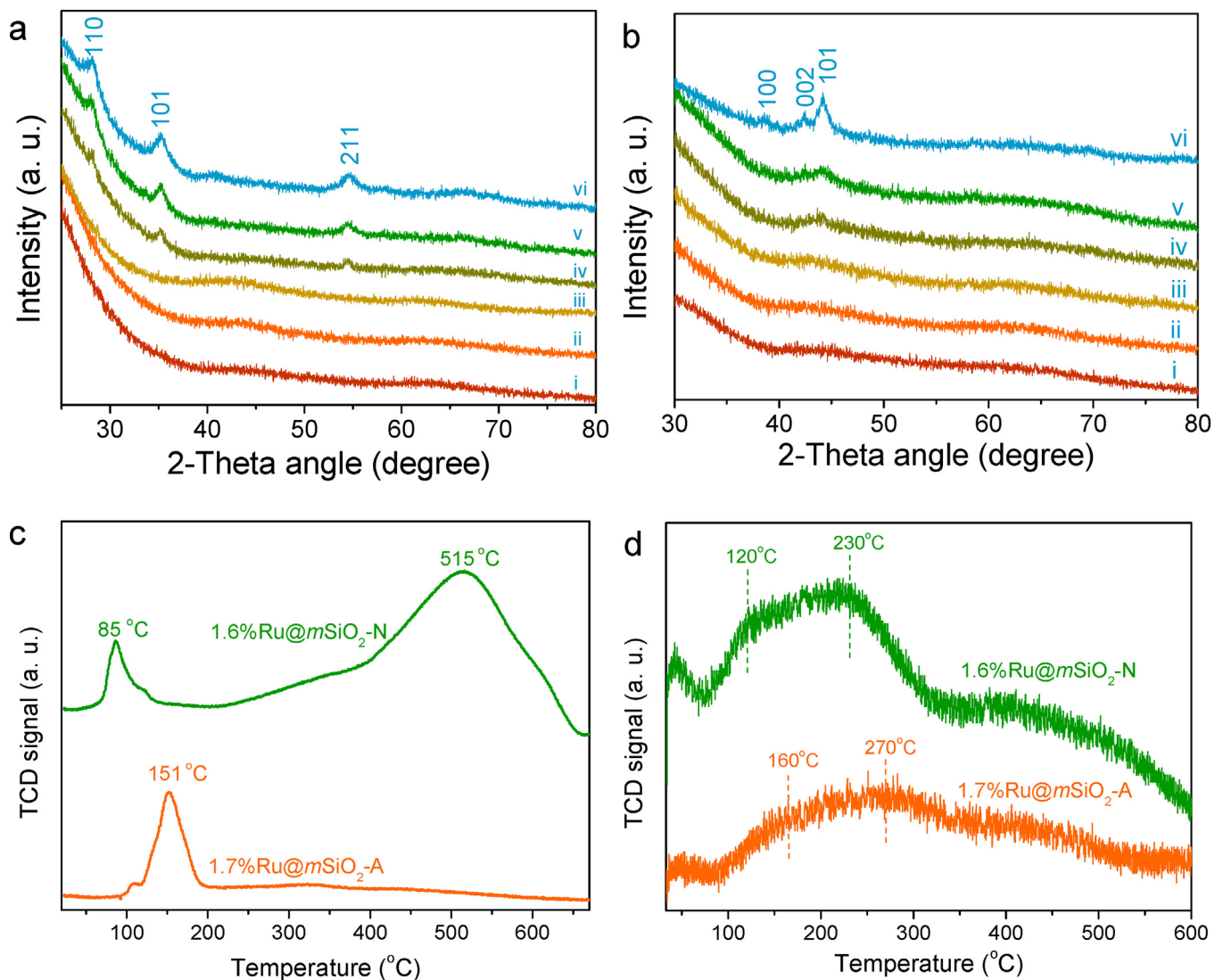


**Fig. 6.** (a) XRD patterns of freshly calcined catalysts: (i) 0.4%Ru@mSiO<sub>2</sub>-N, (ii) 1.6%Ru@mSiO<sub>2</sub>-N, (iii) 2.7%Ru@mSiO<sub>2</sub>-N, (iv) 0.4%Ru@mSiO<sub>2</sub>-A, (v) 1.7%Ru@mSiO<sub>2</sub>-A, and (vi) 3.0%Ru@mSiO<sub>2</sub>-A; the Ru@mSiO<sub>2</sub>-A samples were examined before reduction. (b) XRD patterns of spent catalysts: (i) 0.4%Ru@mSiO<sub>2</sub>-N, (ii) 1.6%Ru@mSiO<sub>2</sub>-N, (iii) 2.7%Ru@mSiO<sub>2</sub>-N, (iv) 0.4%Ru@mSiO<sub>2</sub>-A, (v) 1.7%Ru@mSiO<sub>2</sub>-A, and (vi) 3.0%Ru@mSiO<sub>2</sub>-A. (c) H<sub>2</sub>-TPR and (d) H<sub>2</sub>-TPD profiles of 1.6%Ru@mSiO<sub>2</sub>-N and 1.7%Ru@mSiO<sub>2</sub>-A nanocatalysts.

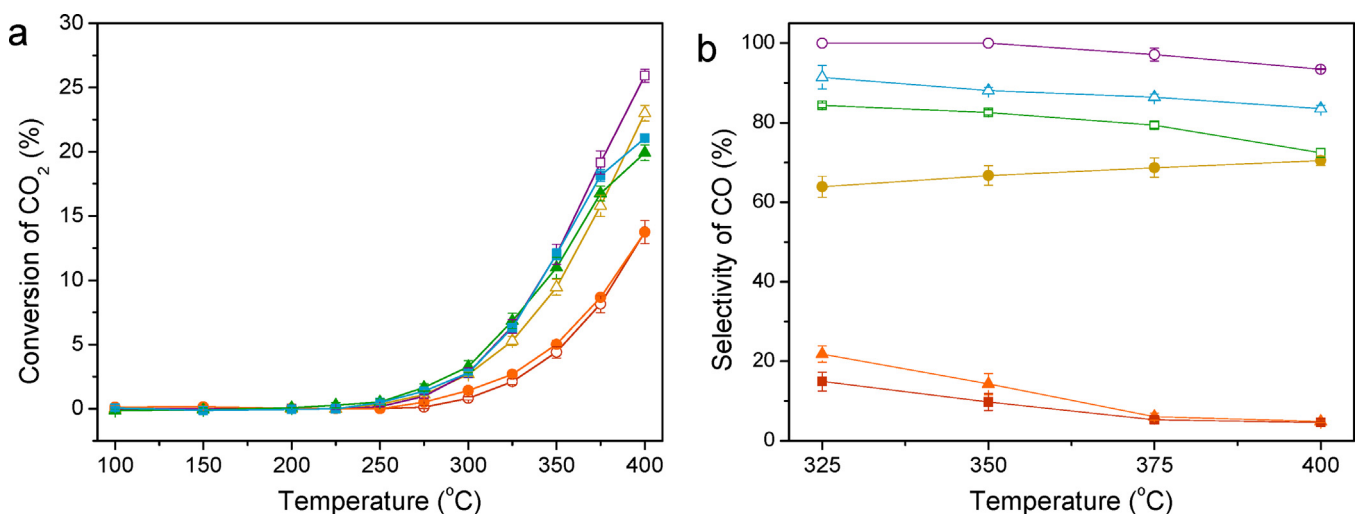


**Fig. 7.** (a) Conversion of CO<sub>2</sub> and (b) selectivity of CO over 0.4%Ru@mSiO<sub>2</sub>-N (open circle), 1.6%Ru@mSiO<sub>2</sub>-N (open triangle), 2.7%Ru@mSiO<sub>2</sub>-N (open square), 0.4%Ru@mSiO<sub>2</sub>-A (filled circle), 1.7%Ru@mSiO<sub>2</sub>-A (filled triangle), and 3.0%Ru@mSiO<sub>2</sub>-A (filled square).

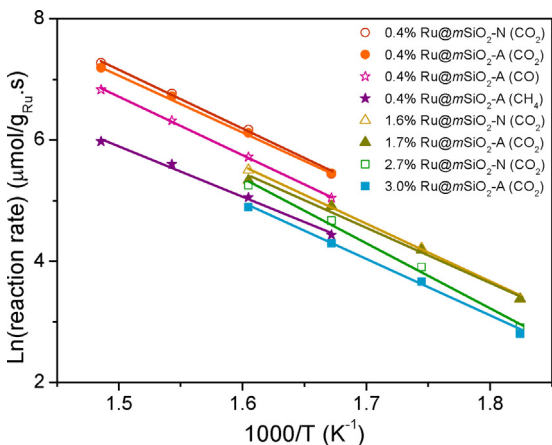


**Fig. 8.** Arrhenius-type plot of 0.4%Ru@mSiO<sub>2</sub>-N (open circle), 1.6%Ru@mSiO<sub>2</sub>-N (open triangle), 2.7%Ru@mSiO<sub>2</sub>-N (open square), 0.4%Ru@mSiO<sub>2</sub>-A (filled circle), 1.7%Ru@mSiO<sub>2</sub>-A (filled triangle), and 3.0%Ru@mSiO<sub>2</sub>-A (filled square) for CO<sub>2</sub> conversion; 0.4%Ru@mSiO<sub>2</sub>-A (open star) for CO formation, and 0.4%Ru@mSiO<sub>2</sub>-A (filled star) for CH<sub>4</sub> formation.

[54] H<sub>2</sub>-TPD analysis was also carried out to examine the affinity of hydrogen to the Ru surfaces. Shown in Fig. 6d, broad hydrogen desorption peaks were observed for 1.6%Ru@mSiO<sub>2</sub>-N and 1.7%Ru@mSiO<sub>2</sub>-A samples. It should be mentioned that the broad desorption peak for 1.6%Ru@mSiO<sub>2</sub>-N catalyst could be due to overlap of two separate peaks at 120 and 230 °C, while that for 1.7%Ru@mSiO<sub>2</sub>-A catalyst could be deconvoluted into two peaks at 160 and 270 °C. The low temperature desorption peak below 200 °C can be assigned to hydrogen bonded onto Ru metal surface, while the high temperature peak at above 200 °C can be attributed to spillover of hydrogen to silica support. [55,56] It suggests that hydrogen binds more strongly on 5–20 nm Ru than on 1–3 nm Ru nanoparticles, which implies that surface coverage of atomic hydrogen (H<sub>a</sub>) is higher on 5–20 nm Ru during reaction.

In order to further understand the difference in reaction selectivity on 1.6%Ru@mSiO<sub>2</sub>-N (1–3 nm Ru) and 1.7%Ru@mSiO<sub>2</sub>-A (5–20 nm Ru) catalysts, *in-situ* diffuse reflectance infrared Fourier transform spectroscopy (DRIFTS) analysis was carried out with 1.6%Ru@mSiO<sub>2</sub>-N and 1.7%Ru@mSiO<sub>2</sub>-A catalysts. As shown in Fig. 9a and b, DRIFTS spectra were measured during hydrogenation of CO<sub>2</sub> at 50–400 °C after adsorption of H<sub>2</sub>/CO<sub>2</sub> mixture (H<sub>2</sub>:CO<sub>2</sub> = 4:1). At 50 °C, only gas phase and/or weak adsorbed CO<sub>2</sub> was observed in DRIFTS spectra for both 1.6%Ru@mSiO<sub>2</sub>-N and 1.7%Ru@mSiO<sub>2</sub>-A catalysts, as evidenced by the strong peak appearing at 2310–2384 cm<sup>-1</sup> (Fig. S15). [11] Increasing the reaction temperature to 100 °C, the DRIFTS spectrum remains almost unchanged for 1.7%Ru@mSiO<sub>2</sub>-A catalyst. However, a small peak was observed at 877 cm<sup>-1</sup> for 1.6%Ru@mSiO<sub>2</sub>-N catalyst, which is attributed surface carbonate species, [57,58] indicating CO<sub>2</sub> chemisorbs on catalyst surface. At 150–400 °C, two broad peaks at 1281 and 1360–1600 cm<sup>-1</sup> appeared, which could be assigned to O–C–O stretching vibration of carboxylate, formate and carbonate species. [11] The four peaks at 877, 964–975, 1001–1004, 1111–1115 cm<sup>-1</sup> observed for both 1.6%Ru@mSiO<sub>2</sub>-N and 1.7%Ru@mSiO<sub>2</sub>-A samples could be assigned to carbonate species (Fig. 9a and 9b). [57,58] Adsorbed CO peaks appeared at 1821–1843 and 1933–1980 cm<sup>-1</sup> for both samples. The peaks in the range of 2810–2957 cm<sup>-1</sup> are attributed to C–H vibration of CH<sub>x</sub> species, while the 3016 cm<sup>-1</sup> peaks are due to CH<sub>4</sub>. [59–61] It is noted that selectivity of CH<sub>4</sub> is 16.5% for 1.6%Ru@mSiO<sub>2</sub>-N at 400 °C, which caused observation of CH<sub>x</sub> and CH<sub>4</sub> peaks in IR spectra. The peaks centered around 3735 cm<sup>-1</sup> and 1673 cm<sup>-1</sup> are attributed to vibration of surface hydroxyl group. [36,59] In order to compare the difference of reaction intermediates formed over 1.6%Ru@mSiO<sub>2</sub>-

N and 1.7%Ru@mSiO<sub>2</sub>-A catalysts, the DRIFTS spectra at 400 °C were presented in the wave number range of 700–2075 cm<sup>-1</sup> and 2075–2250 cm<sup>-1</sup> (Fig. 9c and 9d). For 1.7%Ru@mSiO<sub>2</sub>-A catalyst, characteristic peaks of formate species were observed at 770, 1376 and 1581 cm<sup>-1</sup>, which could be assigned to bending, symmetric and asymmetric stretching vibration of O–C–O group from formate. [57–59,62] However, formate species were not observed over 1.6%Ru@mSiO<sub>2</sub>-N catalyst as the characteristic peaks were absent from its DRIFTS spectrum. On the other hand, by examining the DRIFTS spectra in the 2075–2250 cm<sup>-1</sup> range, it can be seen that two peaks at 2111 and 2176 cm<sup>-1</sup> were observed for 1.6%Ru@mSiO<sub>2</sub>-N catalyst at 350–400 °C (Fig. 9d and S16). These two peaks can be attributed to adsorption of CO on partially oxidized Ru<sup>n+</sup> sites. [63,64] It shall be mentioned that these two peaks at 2111 and 2176 cm<sup>-1</sup> were not observed in the DRIFTS spectra for 1.7%Ru@mSiO<sub>2</sub>-A catalyst. From this *in situ* DRIFTS study, it clearly shows that two types of reaction intermediates formed on the two catalyst surfaces: CO–Ru<sup>n+</sup> on 1.6%Ru@mSiO<sub>2</sub>-N (1–3 nm Ru) and formate species on 1.7%Ru@mSiO<sub>2</sub>-A (5–20 nm Ru). In Fig. 7, it has been demonstrated that CO is selectively produced on 1.6%Ru@mSiO<sub>2</sub>-N, while CH<sub>4</sub> is selectively formed on 1.7%Ru@mSiO<sub>2</sub>-A catalyst. Thus the difference in the selectivity of reaction products (e.g., CO and CH<sub>4</sub>) is closely related to the different reaction intermediates (e.g., CO–Ru<sup>n+</sup> and formate) formed on catalyst surface, which is then related to the difference in the catalyst size (e.g., 1–3 nm Ru and 5–20 nm Ru). As CO–Ru<sup>n+</sup> is observed on 1–3 nm Ru during CO<sub>2</sub> hydrogenation, it is likely that the small Ru nanoparticles could be partially oxidized by CO<sub>2</sub> under the reaction condition at 350–400 °C. It suggests that CO could be directly formed on the surface of small Ru nanoparticles by redox reaction between CO<sub>2</sub> (or surface carbonate) and surface Ru atoms. Through this redox reaction, surface Ru metal was oxidized to Ru<sup>n+</sup>, while CO<sub>2</sub> was reduced to CO and adsorbed onto Ru<sup>n+</sup> sites (surface redox mechanism, Fig. 10a). Owing to low surface coverage of H<sub>a</sub> on 1–3 nm Ru, the surface carbonyl species could desorb directly to release CO gas instead of going on through further hydrogenation steps, while surface atomic oxygen species are cleaned by hydrogen to form water and regenerate the Ru surface. [65,66] As formate species are observed on 1.7%Ru@mSiO<sub>2</sub>-A catalyst surface and CH<sub>4</sub> is the major product, it is thus proposed that CO<sub>2</sub> is hydrogenated through formate to produce the final product of CH<sub>4</sub>. Furthermore, as the activation energy of CO formation is higher than that of CH<sub>4</sub> (Table 1), it is most likely that hydrogen atoms associate with adsorbed CO<sub>2</sub> and generate formate as intermediate species, which is further hydrogenated to CH<sub>4</sub> (formate route, Fig. 10b), instead of through hydrogenation of formed CO species. [59,64,67]

The spent catalysts were characterized by TEM to study morphological changes after reaction. As shown in Fig. 11 and Figs. S17–S22, the general morphology of Ru@mSiO<sub>2</sub>-N and Ru@mSiO<sub>2</sub>-A catalysts remained similar as before the hydrogenation reaction. Powder XRD technique was also used, with results reported in Fig. 6b. Similar to the case of fresh catalysts, there was no XRD peak observed for spent Ru@mSiO<sub>2</sub>-N catalysts. It suggests that the Ru@mSiO<sub>2</sub>-N catalysts are stable under the reaction conditions without sintering of encapsulated Ru nanoparticles, which is also evidenced by TEM observation. For spent Ru@mSiO<sub>2</sub>-A catalysts, the two peaks at 35.3 and 54.5° belonging to RuO<sub>2</sub> disappeared after reaction. Instead a broad peak at 44.2° was observed for spent 0.4%Ru@mSiO<sub>2</sub>-A and 1.7%Ru@mSiO<sub>2</sub>-A catalysts, which is attributed to (101) planes of hexagonal Ru (JCPDS card 06-0663, space group  $P6_3/mmc$ ,  $a_0 = b_0 = 2.705 \text{ \AA}$ , and  $c_0 = 4.281 \text{ \AA}$ ). The (101) peak was more prominent for spent 3.0%Ru@mSiO<sub>2</sub>-A due to higher Ru loading. In addition to the peak at 44.2°, two small peaks at 38.5° and 42.4° were observed, corresponding to (100) and (002) planes of metallic Ru. From XRD analysis, it is known that the RuO<sub>2</sub> in Ru@mSiO<sub>2</sub>-A catalysts has been reduced to Ru metal by hydro-

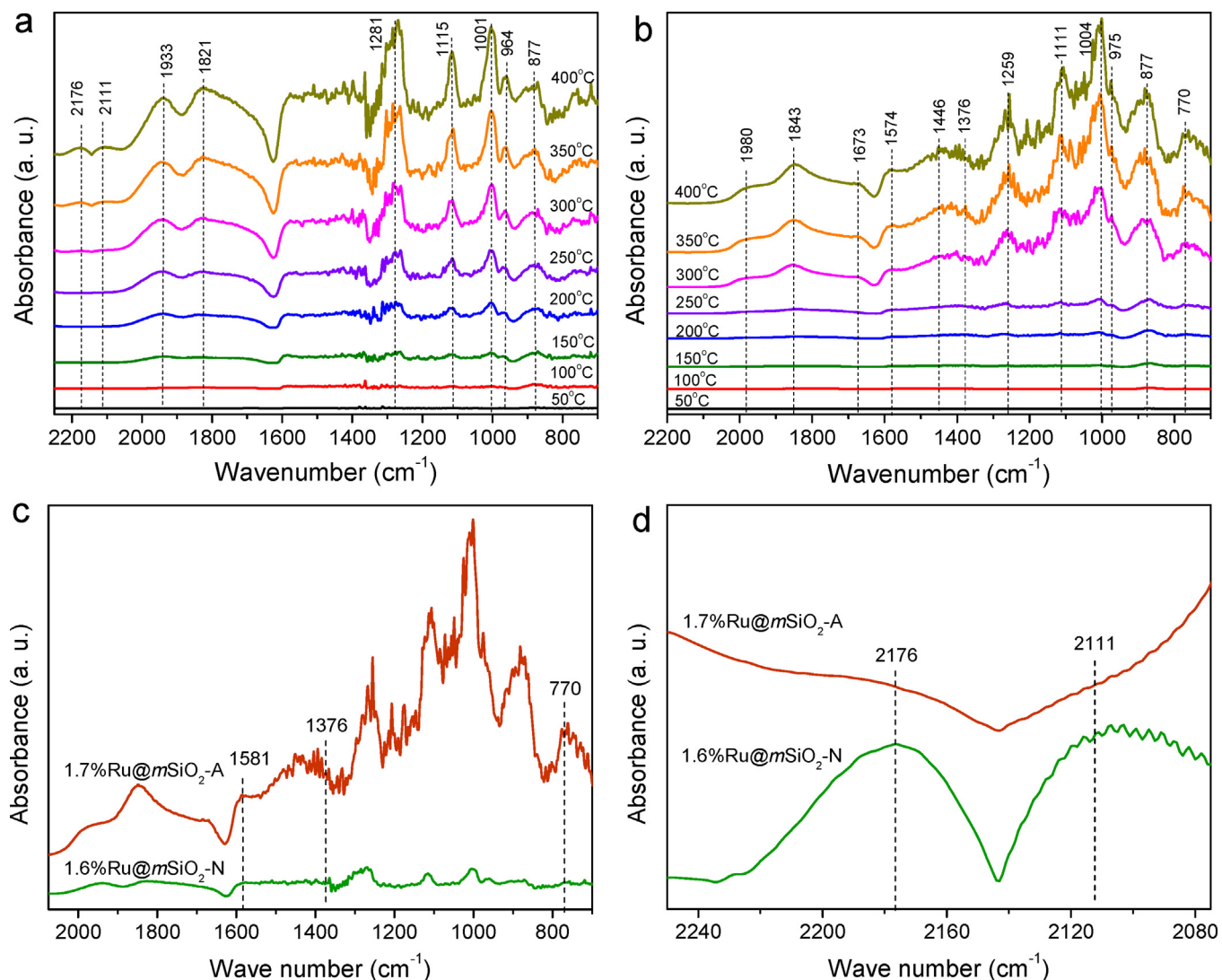


**Fig. 9.** in situ study of selective hydrogenation of CO<sub>2</sub> by DRIFTS on (a) 1.6%Ru@mSiO<sub>2</sub>-N, and (b) 1.7%Ru@mSiO<sub>2</sub>-A catalysts after adsorption of H<sub>2</sub> and CO<sub>2</sub> (H<sub>2</sub>:CO<sub>2</sub> = 4:1) at 50–400 °C; and DRIFTS spectra at 400 °C in the wave number range of (c) 700–2075 cm<sup>-1</sup>, and (d) 2075–2250 cm<sup>-1</sup>.

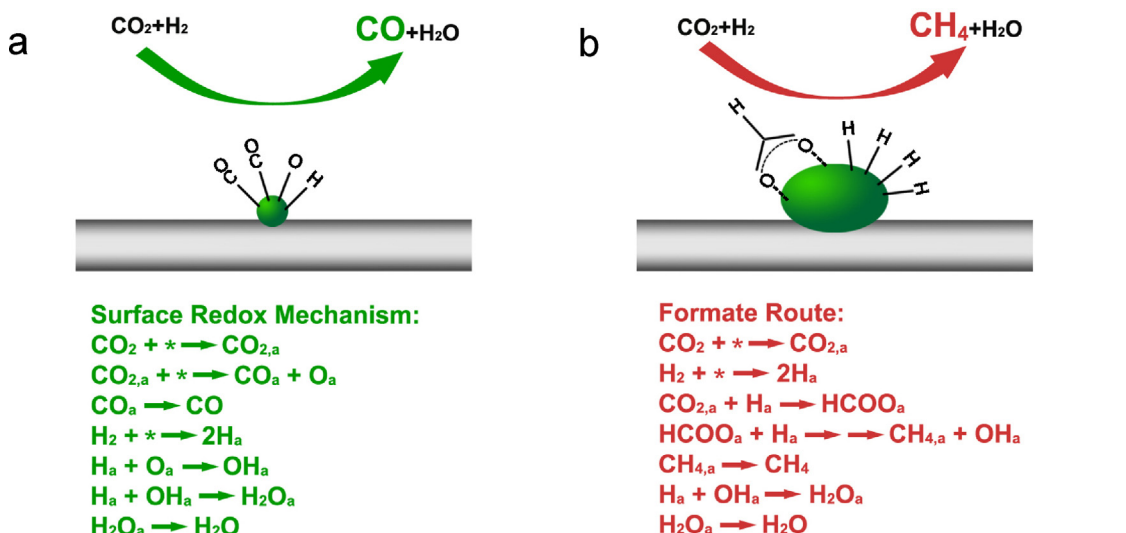


**Fig. 10.** Proposed schemes of (a) surface redox mechanism with 1–3 nm Ru@mSiO<sub>2</sub>, and (b) formate route with 5–20 nm Ru@mSiO<sub>2</sub> nanocatalysts.

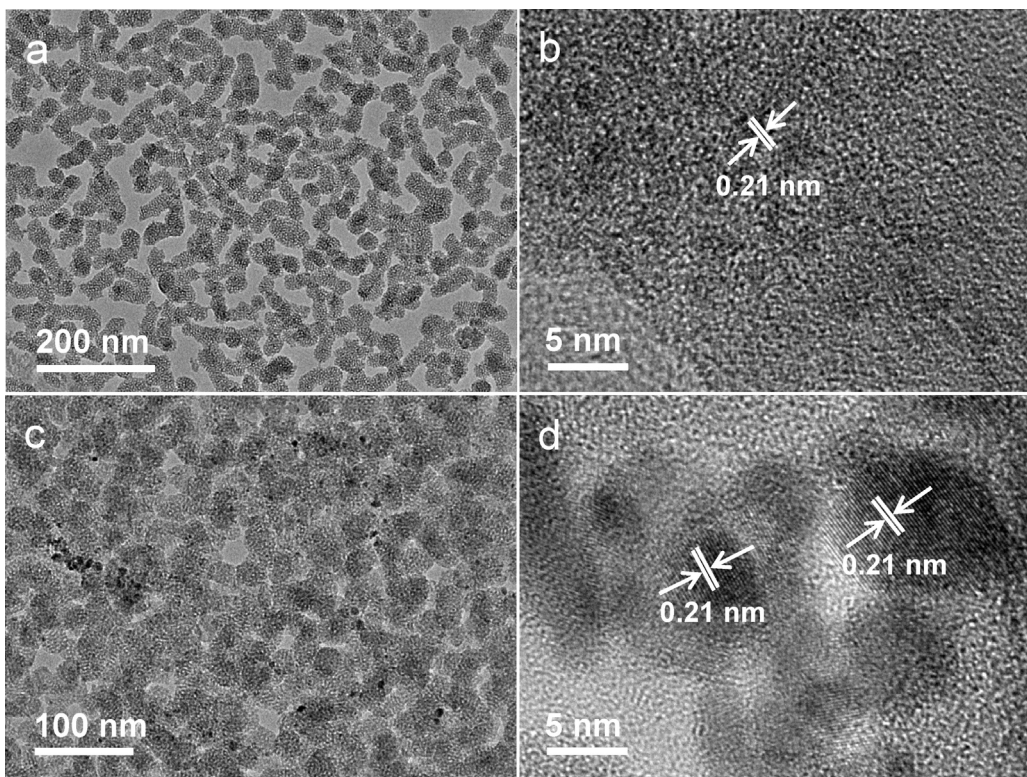


Fig. 11. TEM/HRTEM images of spent catalysts: (a,b) 1.6%Ru@mSiO<sub>2</sub>-N and (c,d) 1.7%Ru@mSiO<sub>2</sub>-A.

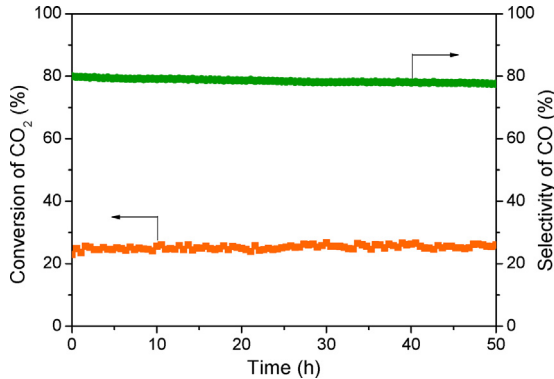


Fig. 12. Stability test of 1.6%Ru@mSiO<sub>2</sub>-N nanocatalyst. Orange line represents conversion of CO<sub>2</sub> and green line stands for selectivity of CO. (For interpretation of the references to colour in this figure legend, the reader is referred to the web version of this article.)

gen after reaction. The oxidation states of Ru in the used catalysts were further studied by XPS analysis (Figs. S23 and S24). Referenced to Si 2p at 103.3 eV, the Ru 3p<sub>3/2</sub> binding energy of spent 1.7%Ru@mSiO<sub>2</sub>-A catalyst was measured as 461.6 eV corresponding to reduced Ru(0). For spent 1.6%Ru@mSiO<sub>2</sub>-N catalyst, the Ru 3p<sub>3/2</sub> binding energy at 462.1 eV is slightly higher than that of the fresh catalyst (Ru 3p<sub>3/2</sub> = 461.8 eV) and spent 1.7%Ru@mSiO<sub>2</sub>-A catalysts. It supports the previous discussion that surface coverage of atomic hydrogen is higher on 1.7%Ru@mSiO<sub>2</sub>-A sample, leading to a more reduced state of Ru.

The Ru@mSiO<sub>2</sub>-N catalysts have been demonstrated to be very stable by extended reaction test at 400 °C and 500 °C for 50 h (Figs. 12, S25 and S26). Displayed in Fig. 12, the average conversion of CO<sub>2</sub> during initial 2 h of reaction for 1.6%Ru@mSiO<sub>2</sub>-N catalyst was 24.2%, which gradually increased to 25.7% at the end of the 50 h reaction at 400 °C. The CO selectivity was measured as 79.7%

initially and only dropped slightly to 77.6% at the end. Increasing the reaction to 500 °C, the conversion of CO<sub>2</sub> and selectivity of CO at 2 h of reaction is 54.6% and 66.7%, respectively. At the 50 h of reaction, the conversion of CO<sub>2</sub> and selectivity of CO remains almost unchanged as 56.5% and 66.0%, accordingly. It shows that the Ru@mSiO<sub>2</sub>-N is stable during RWGS reaction at 400–500 °C. Furthermore, the size of Ru nanoparticles remains unchanged at 1–3 nm after the reaction (Fig. S27), which further confirms the effectiveness of mesoporous silica support to stabilize Ru nanoparticles during reaction.

#### 4. Conclusions

In summary, Ru-loaded mesoporous silica nanowires as a novel nanocatalyst were synthesized successfully by simultaneous hydrolysis/condensation of TEOS and encapsulation of pre-synthesized Ru nanoparticles. Calcination in N<sub>2</sub> was found effective in preventing the encapsulated Ru nanoparticles (1–3 nm) from sintering. In contrast, oxidative sintering of the Ru nanoparticles occurred with calcination in air, resulting in 5–20 nm Ru nanocrystals after activation with H<sub>2</sub>/CO<sub>2</sub>. CO<sub>2</sub> hydrogenation experiments showed high (up to 100%) CO selectivity with the 1–3 nm Ru@mSiO<sub>2</sub> catalysts calcined in N<sub>2</sub> but high CH<sub>4</sub> selectivity with the 5–20 nm Ru@mSiO<sub>2</sub> catalysts calcined in air, which demonstrates the crucial role of particle size control in optimizing catalytic performance. The high selectivity of CO over CH<sub>4</sub> was attributed to low affinity and hence coverage of atomic hydrogen on the surface of the 1–3 nm Ru nanoparticles. DRIFTS, TPR and TPD experiments supported a surface redox mechanism for CO<sub>2</sub> hydrogenation on 1–3 nm Ru@mSiO<sub>2</sub>, where carbonyl species form by dissociative adsorption of CO<sub>2</sub> and desorb directly to generate CO. With 5–20 nm Ru@mSiO<sub>2</sub> catalysts, a formate route was established where adsorbed atomic hydrogen associates with adsorbed CO<sub>2</sub> to form formate species which are further hydrogenated to CH<sub>4</sub> with sufficient supply of surface hydrogen atoms. In addition,

the Ru@mSiO<sub>2</sub>-N catalyst has been proven very stable in terms of activity and selectivity within extended reaction time of 50 h. The present bottom-up fabrication method of nanocatalysts facilitates future study on structure–performance relation of supported catalysts, and the attractive properties of our Ru nanocatalysts suggest promising applications in CO<sub>2</sub> utilization.

## Acknowledgment

The authors gratefully acknowledge the financial support provided by the Ministry of Education, Singapore, NUS, and GSK Singapore. This project is also partially funded by the National Research Foundation (NRF), Prime Minister's Office, Singapore under its Campus for Research Excellence and Technological Enterprise (CREATE) program.

## Appendix A. Supplementary data

Supplementary data associated with this article can be found, in the online version, at <http://dx.doi.org/10.1016/j.apcatb.2017.07.083>.

## References

- [1] W. Wang, S. Wang, X. Ma, J. Gong, *Chem. Soc. Rev.* 40 (2011) 3703–3727.
- [2] C. Song, *Catal. Today* 115 (2006) 2–32.
- [3] H. Arakawa, M. Areata, J.N. Armor, M.A. Barteeau, E.J. Beckman, A.T. Bell, J.E. Bercaw, C. Creutz, E. Dinjus, D.A. Dixon, K. Domen, D.L. DuBois, J. Eckert, E. Fujita, D.H. Gibson, W.A. Goddard, D.W. Goodman, J. Keller, G.J. Kubas, H.H. Kung, J.E. Lyons, L.E. Manzer, T.J. Marks, K. Morokuma, K.M. Nicholas, R. Periana, L. Que, J. Rostrup-Nielsen, W.M.H. Sachtleber, L.D. Schmidt, A. Sen, G.A. Somorjai, P.C. Stair, B.R. Stults, W. Tumas, *Chem. Rev.* 101 (2001) 953–996.
- [4] X. Xu, J.A. Moulijn, *Energy Fuels* 10 (1996) 305–325.
- [5] M. Behrens, F. Studt, I. Kasatkin, S. Kuhl, M. Havecker, F. Abild-Pedersen, S. Zander, F. Girsides, P. Kurr, B.L. Kniep, M. Tovar, R.W. Fischer, J.K. Norskov, R. Schlogl, *Science* 336 (2012) 893–897.
- [6] F. Arena, G. Mezzatesta, G. Zafarana, G. Trunfio, F. Frusteri, L. Spadaro, *J. Catal.* 300 (2013) 141–151.
- [7] S.-W. Park, O.-S. Joo, K.-D. Jung, H. Kim, S.-H. Han, *Appl. Catal. A* 211 (2001) 81–90.
- [8] M.J.L. Ginés, A.J. Marchi, C.R. Pesteguía, *Appl. Catal. A* 154 (1997) 155–171.
- [9] C.S. Chen, W.H. Cheng, S.S. Lin, *Appl. Catal. A* 257 (2004) 97–106.
- [10] C.S. Chen, J.H. Lin, J.H. You, C.R. Chen, *J. Am. Chem. Soc.* 128 (2006) 15950–15951.
- [11] A. Goguet, F.C. Meunier, D. Tibiletti, J.P. Breen, R. Burch, *J. Phys. Chem. B* 108 (2004) 20240–20246.
- [12] S.S. Kim, H.H. Lee, S.C. Hong, *Appl. Catal. B* 119–120 (2012) 100–108.
- [13] J.H. Kwak, L. Kovarik, J. Szanyi, *ACS Catal.* 3 (2013) 2094–2100.
- [14] J.C. Matsubu, V.N. Yang, P. Christopher, *J. Am. Chem. Soc.* 137 (2015) 3076–3084.
- [15] X. Wang, H. Shi, J.H. Kwak, J. Szanyi, *ACS Catal.* 5 (2015) 6337–6349.
- [16] J.-N. Park, E.W. McFarland, *J. Catal.* 266 (2009) 92–97.
- [17] H.C. Wu, Y.C. Chang, J.H. Wu, J.H. Lin, I.K. Lin, C.S. Chen, *Catal. Sci. Technol.* 5 (2015) 4154–4163.
- [18] F.-W. Chang, M.-S. Kuo, M.-T. Tsay, M.-C. Hsieh, *Appl. Catal. A* 247 (2003) 309–320.
- [19] G. Du, S. Lim, Y. Yang, C. Wang, L. Pfefferle, G.L. Haller, *J. Catal.* 249 (2007) 370–379.
- [20] C. Li, S. Zhang, B. Zhang, D. Su, S. He, Y. Zhao, J. Liu, F. Wang, M. Wei, D.G. Evans, X. Duan, *J. Mater. Chem. A* 1 (2013) 2461–2467.
- [21] Y. Zhu, S. Zhang, Y. Ye, X. Zhang, L. Wang, W. Zhu, F. Cheng, F. Tao, *ACS Catal.* 2 (2012) 2403–2408.
- [22] S. Sharma, Z. Hu, P. Zhang, E.W. McFarland, H. Metiu, *J. Catal.* 278 (2011) 297–309.
- [23] T. Abe, M. Tanizawa, K. Watanabe, A. Taguchi, *Energy Environ. Sci.* 2 (2009) 315–321.
- [24] X. Zhang, X. Zhu, L. Lin, S. Yao, M. Zhang, X. Liu, X. Wang, Y.-W. Li, C. Shi, D. Ma, *ACS Catal.* 7 (2017) 912–918.
- [25] C.Á. Galván, J. Schumann, M. Behrens, J.L.G. Fierro, R. Schlogl, E. Frei, *Appl. Catal. B* 195 (2016) 104–111.
- [26] R.V. Gonçalves, L.R. Vono, R. Wojcieszak, C.S.B. Dias, H. Wender, E. Teixeira-Neto, L.M. Rossi, *Appl. Catal. B* 209 (2017) 240–246.
- [27] V. Srivastava, *Catal. Lett.* 146 (2016) 2630–2640.
- [28] R. Carrasquillo-Flores, I. Ro, M.D. Kumbhalkar, S. Burt, C.A. Carrero, A.C. Alba-Rubio, J.T. Miller, I. Hermans, G.W. Huber, J.A. Dumesic, *J. Am. Chem. Soc.* 137 (2015) 10317–10325.
- [29] I. Ro, C. Sener, T.M. Stadelman, M.R. Ball, J.M. Venegas, S.P. Burt, I. Hermans, J.A. Dumesic, G.W. Huber, *J. Catal.* 344 (2016) 784–794.
- [30] A. Goguet, F. Meunier, J.P. Breen, R. Burch, M.I. Petch, A.F. Ghenciu, *J. Catal.* 226 (2004) 382–392.
- [31] S. Choi, B.-I. Sang, J. Hong, K.J. Yoon, J.-W. Son, J.-H. Lee, B.-K. Kim, H. Kim, *Sci. Rep.* 7 (2017) 41207.
- [32] D.H. Kim, J.L. Park, E.J. Park, Y.D. Kim, S. Uhm, *ACS Catal.* 4 (2014) 3117–3122.
- [33] K. Tsuchiya, J.-D. Huang, K. Tominaga, *ACS Catal.* 3 (2013) 2865–2868.
- [34] K. Tominaga, Y. Sasaki, K. Haghjara, T. Watanabe, M. Saito, *Chem. Lett.* (1994) 1391–1394.
- [35] M.M.T. Khan, S.B. Halligudi, S. Shukla, *J. Mol. Catal.* 57 (1989) 47–60.
- [36] S. Scirè, C. Crisafulli, R. Maggiore, S. Minicò, S. Galvagno, *Catal. Lett.* 51 (1998) 41–45.
- [37] J.H. Kwak, L. Kovarik, J. Szanyi, *ACS Catal.* 3 (2013) 2449–2455.
- [38] C. Jiang, K. Hara, A. Fukuoka, *Angew. Chem. Int. Ed.* 52 (2013) 6265–6268.
- [39] Y. Wan, D. Zhao, *Chem. Rev.* 107 (2007) 2821–2860.
- [40] K.X. Yao, H.C. Zeng, *Chem. Mater.* 24 (2012) 140–148.
- [41] Y. Wang, J. Ren, K. Deng, L. Gui, Y. Tang, *Chem. Mater.* 12 (2000) 1622–1627.
- [42] J. Dou, H.C. Zeng, *ACS Catal.* 4 (2014) 566–576.
- [43] R. Ouyang, J.-X. Liu, W.-X. Li, *J. Am. Chem. Soc.* 135 (2013) 1760–1771.
- [44] S.B. Simonsen, I. Chorkendorff, S. Dahl, M. Skoglundh, J. Sehested, S. Helveg, *J. Am. Chem. Soc.* 132 (2010) 7968–7975.
- [45] P.I. Ravikovich, S.C. Ó Domhnaill, A.V. Neimark, F. Schüth, K.K. Unger, *Langmuir* 11 (1995) 4765–4772.
- [46] J.Y. Shen, A. Adnot, S. Kaliaguine, *Appl. Surf. Sci.* 51 (1991) 47–60.
- [47] C.-S. Chen, W.-H. Cheng, S.-S. Lin, *Appl. Catal. A* 238 (2003) 55–67.
- [48] S.S. Kim, H.H. Lee, S.C. Hong, *Appl. Catal. A* 423–424 (2012) 100–107.
- [49] X. Chen, X. Su, H. Duan, B. Liang, Y. Huang, T. Zhang, *Catal. Today* 281 (2017) 312–318.
- [50] H. Xu, Y. Li, X. Luo, Z. Xu, J. Ge, *Chem. Commun.* (2017), <http://dx.doi.org/10.1039/C7CC02130E>.
- [51] G.D. Weatherbee, C.H. Bartholomew, *J. Catal.* 87 (1984) 352–362.
- [52] L. Ma, D.H. He, *Catal. Today* 149 (2010) 148–156.
- [53] E.B. Pereira, N. Homs, S. Martí, J.L.G. Fierro, P. Ramírez de la Piscina, *J. Catal.* 257 (2008) 206–214.
- [54] M.D. Argyle, C.H. Bartholomew, *Catalysts* 5 (2015) 145–269.
- [55] L.H. Yao, Y.X. Li, J. Zhao, W.J. Ji, C.T. Au, *Catal. Today* 158 (2010) 401–408.
- [56] H.-Y. Lin, Y.-W. Chen, *Thermochim. Acta* 419 (2004) 283–290.
- [57] T. Tabakova, F. Bocuzzi, M. Manzoli, D. Andreeva, *Appl. Catal. A* 252 (2003) 385–397.
- [58] C. Binet, M. Daturi, J.-C. Lavalle, *Catal. Today* 50 (1999) 207–225.
- [59] M. Marwood, R. Doepper, A. Renken, *Appl. Catal. A* 151 (1997) 223–246.
- [60] C. Choong, Z. Zhong, L. Huang, A. Borgna, L. Hong, L. Chen, J. Lin, *ACS Catal.* 4 (2014) 2359–2363.
- [61] N.M. Gupta, V.S. Kamble, V.B. Kartha, R.M. Iyer, K.R. Thampi, M. Grätzel, *J. Catal.* 146 (1994) 173–184.
- [62] C. Li, K. Domen, K. Maruya, T. Onishi, *J. Catal.* 125 (1990) 445–455.
- [63] P. Panagiotopoulou, D.I. Kondarides, X.E. Verykios, *J. Phys. Chem. C* 115 (2011) 1220–1230.
- [64] M.R. Prairie, A. Renken, J.G. Highfield, K.R. Thampi, M. Grätzel, *J. Catal.* 129 (1991) 130–144.
- [65] K.-H. Ernst, C.T. Campbell, G. Moretti, *J. Catal.* 134 (1992) 66–74.
- [66] S. Fujita, M. Usui, N. Takezawa, *J. Catal.* 134 (1992) 220–225.
- [67] P. Panagiotopoulou, D.I. Kondarides, X.E. Verykios, *Catal. Today* 181 (2012) 138–147.